Trop J Nat Prod Res, December 2025; 9(12): 5964 - 5972

**ISSN 2616-0684 (Print)**
**ISSN 2616-0692 (Electronic)**

# Tropical Journal of Natural Product Research

Available online at https://www.tjnpr.org

*Original Research Article*

# Structure-Based Identification and Dynamic Profiling of *Mitragyna speciosa* Metabolites Targeting HPV E6 and EBNA1 in Cervical Cancer

Nabila H. Akbar[1]*, Putri H. J. Buih[1], Khoirunnisa M.[1], Farendina S.[2], Aditya M. P. Putra[3], Muhammad F. Hakiki[4], Muhammad A. Q. Salim[4], and Taufik M. Fakih[4]

[1]*Pharmacist Professional Education Study Program (PPSP), Faculty of Mathematics and Natural Sciences, Universitas Lambung Mangkurat, Jl. A. Yani, Banjarmasin 70123, Indonesia*
[2]*Pharmacist Professional Education Study Program (PPSP), Faculty of Mathematics and Natural Sciences, Universitas Islam Bandung, Jl. Ranggagading, Bandung 40116, Indonesia*
[3]*Department of Pharmacy, Faculty of Mathematics and Natural Sciences, Universitas Lambung Mangkurat, Jl. A. Yani, Banjarmasin 70123, Indonesia*
[4]*Department of Pharmacy, Faculty of Mathematics and Natural Sciences, Universitas Islam Bandung, Jl. Ranggagading, Bandung 40116, Indonesia*

ARTICLE INFO

*Article history:*
Received 01 August 2025
Revised 20 November 2025
Accepted 21 November 2025
Published online 01 January 2026



ABSTRACT

Cervical cancer remains the fourth most commonly diagnosed malignancy and a leading cause of cancer-related mortality among women worldwide. Persistent infection with high-risk human papillomaviruses (HPVs), particularly types 16 and 18, is recognized as the primary etiological factor. Moreover, accumulating evidence suggests that co-infection with Epstein–Barr virus (EBV) may exacerbate cervical cancer progression, likely through the synergistic disruption of host cellular control mechanisms. The viral oncoproteins HPV E6 and Epstein–Barr nuclear antigen 1 (EBNA1) play pivotal roles in carcinogenesis by inactivating tumor suppressor pathways and maintaining viral genomes within host cells. Consequently, these proteins represent attractive molecular targets for the development of antiviral therapeutics aimed at virus-driven malignancies. In this study, a structure-based virtual screening approach was employed to evaluate 50 phytometabolites derived from *Mitragyna speciosa* against three key viral targets: HPV16 E6 (PDB ID: 6SJV) and two crystal structures of EBNA1 (PDB IDs; 6VH6 and 6NPP), respectively. Molecular docking using AutoDock Vina via AutoDock Tools facilitated the identification of the top five ligands with the most favorable binding affinities. These were further subjected to detailed interaction analysis, *in silico* pharmacokinetic assessment using SwissADME, and oral toxicity prediction via the ProTox-II platform. Among the shortlisted compounds, *β*-Stigmasterol and oleanolic acid emerged as the most promising candidates based on their superior binding energies, favorable ADME profiles, and acceptable predicted safety margins. Collectively, these findings support the therapeutic potential of selected *Mitragyna speciosa* metabolites as dual-target inhibitors of EBV and HPV oncoproteins, offering a valuable framework for future antiviral drug development.

***Keywords:*** *Mitragyna speciosa*, Human papillomaviruses E6, Epstein–Barr nuclear antigen 1, Cervical cancer, Molecular modeling.

## Introduction

Viruses are well-recognized contributors to the development of several human cancers, with human papillomavirus (HPV) and Epstein–Barr virus (EBV) among the most studied oncogenic viruses. [1] Globally, cancers associated with viral infections account for an estimated 10–15% of all cancer cases, demonstrating their significant public health impact. Within this category, HPV and EBV together are responsible for approximately 38% of tumor-associated malignancies, underscoring their high. [2,3] Cervical cancer stands as one of the most common and lethal cancers in women, particularly in low- and middle-income countries. This burden is predominantly driven by persistent infection with high-risk HPV strains, notably HPV-16 and HPV-18. [4] .

*Corresponding author. Email: nabilahadiahakbar@ulm.ac.id
Tel: +62 813-1132-8401

Citation: Akbar NH, Buih PHJ, Muslimawati K, Suarantika F, Putra AMP, Hakiki MF, Salim MAQ, Fakih TM. Structure-Based Identification and Dynamic Profiling of *Mitragyna speciosa* Metabolites Targeting HPV E6 and EBNA1 in Cervical Cancer. Trop J Nat Prod Res. 2025; 9(12): 5964 – 5972 https://doi.org/10.26538/tjnpr/v9i12.8

Official Journal of Natural Product Research Group, Faculty of Pharmacy, University of Benin, Benin City, Nigeria

These viral types are known for their strong oncogenic potential, leading to the progression from precancerous lesions to invasive carcinomaWhile HPV is the primary etiological agent of cervical cancer, EBV has also been implicated in a range of malignancies. [5,6] Importantly, both viruses have been observed to co-infect cervical tissues, potentially influencing cancer severity and progression. EBV is classically linked to nasopharyngeal carcinoma and various lymphomas, but evidence now suggests its role in cervical carcinogenesis as well. [7] Co-infection with HPV and EBV may exacerbate oncogenic pathways, possibly through synergistic effects on immune evasion and cell cycle deregulation. HPV expresses oncoproteins such as E6 and E7, which disrupt key tumor suppressor pathways in host cells. [8,9] In particular, the E6 protein facilitates the degradation of the p53 tumor suppressor through its interaction with the E6-associated protein (E6AP), a ubiquitin ligase. [10] EBV, on the other hand, produces EBNA1, a nuclear antigen essential for viral genome replication and episome maintenance in infected cells. EBNA1 is critical for viral persistence and contributes to host genome instability. [11,12] Targeting these viral proteins offers an attractive approach for therapeutic intervention, as they are central to viral survival and oncogenesis. However, no current antiviral agents that specifically inhibit EBNA1 or HPV E6, representing an unmet medical need. Existing treatment options for virus-associated cancers are largely non-specific and often fail to address the underlying viral mechanisms. Conventional therapies such as chemotherapy and radiotherapy can be

effective but are associated with significant toxicity and relapse rates. [13,14] There is growing interest in developing direct-acting antivirals that can inhibit essential viral proteins involved in carcinogenesis. For HPV and EBV, therapeutic strategies targeting E6 and EBNA1 could disrupt viral persistence and impair tumor progression. Furthermore, drug discovery is increasingly exploring polypharmacological approaches, which aim to modulate multiple molecular targets simultaneously. [15] This strategy is particularly beneficial for complex diseases like cancer, where multiple pathways are dysregulated. In the case of HPV and EBV co-infection, multitarget agents could theoretically address both viral infections within the same therapeutic framework. Such approaches have the potential to improve efficacy, reduce resistance, and minimize adverse effects. Natural products have long been recognized as valuable sources of bioactive compounds for drug discovery. They provide a structurally diverse chemical space that can yield unique scaffolds for therapeutic development. Many plant-derived compounds have demonstrated potent anticancer and antiviral properties with favorable safety profiles. [16,17] *Mitragyna speciosa*, commonly known as kratom, is a medicinal plant traditionally used in Southeast Asia for its analgesic and stimulant effects. [18] Beyond its ethnomedicinal uses, *Mitragyna speciosa* contains a wide array of secondary metabolites, including alkaloids and flavonoids, which may exhibit anticancer activity. [19,20] Some studies have reported its potential in modulating immune function and inhibiting tumor growth. [21,22] However, research exploring its chemical constituents for virus-associated cancer therapy remains limited. This gap presents an opportunity to investigate its metabolites as potential multitarget agents against HPV E6 and EBNA1. Advances in computational tools have facilitated the rapid identification of promising drug candidates from natural sources. Structure-based virtual screening methods, such as molecular docking enable the prediction of binding affinities between small molecules and target proteins. This approach allows researchers to prioritize compounds with strong theoretical interactions for further evaluation. Additionally, pharmacokinetic profiling using ADMET (absorption, distribution, metabolism, excretion, and toxicity) analysis can assess drug-likeness properties early in the discovery process. Toxicity prediction tools help eliminate candidates with undesirable safety profiles before entering experimental stages. In this study, molecular docking was applied to evaluate the interaction of selected *Mitragyna speciosa* metabolites with HPV E6 and EBNA1. Molecular docking, ADME simulation, toxicity prediction, and molecular dynamics simulation were performed to achieve a rigorous prioritization of metabolites based on binding affinity, pose stability, and safety-relevant properties. The top-ranked compounds were then analyzed for pharmacokinetic characteristics and oral toxicity potential. This integrative *in silico* approach aimed to identify safe and effective natural product-derived candidates for managing virus-associated cervical cancer

## Materials and Methods

*Ligand Preparation*

A total of 50 natural metabolites from *Mitragyna speciosa* were retrieved from the KNApSAcK database in SMILES format. [23] These structures were converted into three-dimensional (3D) structures using the Chem3D v21.0.1 (PerkinElmer Inc., USA, 2021) software. [24] Geometry optimization was performed using the MM2 force field to obtain the lowest-energy conformation. Each optimized structure was saved in .mol2 format for further use in docking. Open Babel v3.1.1 (Open Babel Developers, 2020) was then employed to convert the .mol2 files into .pdbqt format compatible with AutoDock Vina v1.2.3 (Center for Computational Structural Biology, Scripps Research, USA; 2021). [25] Protonation states were adjusted to pH 7.4, and Gasteiger charges were assigned to each ligand. All torsional bonds were set as rotatable except those in ring systems. AutoDock Tools v1.5.7 (The Scripps Research Institute, USA, 2014) was also used to validate torsion and charge assignments. [26] A visual inspection was conducted to ensure that no atoms were missing or structural distorted. All ligands were stored in a single folder for batch processing. Selected ligands for advanced evaluation were chosen based on their docking scores and interaction profiles.

*Protein Preparation*

Three crystal structures were selected as protein targets: EBNA1 (PDB IDs: 6VH6 and 6NPP) and HPV E6 (PDB ID: 6SJV). [27,28] The PDB files were downloaded from the RCSB Protein Data Bank. Water molecules, ligands, and heteroatoms were removed using BIOVIA Discovery Studio Visualizer v21.1 (Dassault Systèmes, France, 2021). [29] Polar hydrogens were added and Kollman charges were assigned using AutoDock Tools v1.5.7 (The Scripps Research Institute, USA, 2014). The protein structures were then converted into .pdbqt format for docking. Grid box parameters were defined to encompass the entire active site based on co-crystallized ligand positions or literature-reported residues. The grid dimensions were uniformly set to 64 × 60 × 60 Å with a spacing of 1.0 Å. Grid center coordinates were optimized to cover the putative binding pocket. The prepared proteins were visually inspected to ensure structural integrity. Each target protein was saved as an individual .pdbqt file. These files were then used for docking simulation using AutoDock Vina v1.2.3 (Center for Computational Structural Biology, Scripps Research, USA; 2021). All proteins were processed under the same protocol to ensure consistency.

*Molecular Docking Study*

Docking simulations were conducted using AutoDock Vina v1.2.3 (Center for Computational Structural Biology, Scripps Research, USA; 2021) with default exhaustiveness set to 8 and 100 docking runs for each ligand–protein complex to ensure sampling robustness. Each ligand was docked separately to the three protein targets. The output .pdbqt files from ligand and protein preparation were input into the docking script. The docking results were ranked based on binding affinity (kcal/mol), and the top-ranked conformation was selected for each complex. Visualization and interaction profiling were performed using BIOVIA Discovery Studio Visualizer v21.1 (Dassault Systèmes, France, 2021). Hydrogen bonding and hydrophobic contacts were recorded in detail. To confirm binding results, AutoDock Tools v1.5.7 (The Scripps Research Institute, USA, 2014 with Lamarckian Genetic Algorithm was also employed on the five prioritized compounds. This dual approach helped verify docking consistency across software. Inhibition constants (Ki) were calculated using AutoDock Tools v1.5.7 (The Scripps Research Institute, USA, 2014 based on docking energies. Docked complexes were also evaluated for the presence of key residues involved in stabilizing interactions.

*ADME and Bioavailability Analysis*

Pharmacokinetic profiling of the selected compounds was conducted using the SwissADME (Swiss Institute of Bioinformatics, Switzerland, 2019 release) online platform. [30] Canonical SMILES strings of each metabolite were entered individually into the web-based interface. SwissADME computed a range of ADME-related parameters for each compound. These included Topological Polar Surface Area (TPSA), consensus LogP, gastrointestinal (GI) absorption, and blood–brain barrier (BBB) permeability. Solubility classification was predicted using the ESOL model integrated within the platform. The tool also provided information on whether each compound is a substrate of P-glycoprotein (P-gp), which can affect drug efflux. Bioavailability scores were automatically generated based on each compound's physicochemical profile. In addition to numerical data, SwissADME produced bioavailability radar plots for visual interpretation. These radar plots display six properties: lipophilicity (LIPO), size (SIZE), polarity (POLAR), solubility (INSOLU), saturation (INSATU), and flexibility (FLEX). Each property is compared against a predefined optimal range for oral bioavailability.

*Toxicity Prediction*

*In silico* oral toxicity prediction was conducted to evaluate the potential safety profile of selected metabolites. The analysis was carried out using ProTox-II (Charité – Universitätsmedizin Berlin, Germany, 2020 release), an online prediction tool. [31] Canonical SMILES of each compound were submitted through the web interface for batch processing. The platform utilizes machine learning algorithms trained on toxicological databases to estimate $LD_{50}$ values and toxicity classes. $LD_{50}$ values were predicted in mg/kg, representing the median lethal dose in rodent models. Each compound was also classified into one of

ISSN 2616-0684 (Print)
ISSN 2616-0692 (Electronic)

six toxicity classes based on the Globally Harmonized System (GHS). The prediction output included similarity scores between the test compound and known toxicants in the training dataset. In addition, the tool provided prediction accuracy percentages to indicate the confidence level of each classification. Structural alerts and probable mechanisms of toxicity were generated when applicable.

*MD Simulations and Binding Free Energy Calculations*

Molecular dynamics (MD) simulations were performed to assess the structural stability and interaction dynamics of native-ligand and metabolite-ligand complexes with target proteins EBNA1 (PDB IDs: 6VH6, 6NPP) and HPV E6 (PDB ID: 6SJV). All protein-ligand complexes were initially prepared by docking using AutoDock Vina, followed by selection of the best-ranked poses for MD input. The simulations were conducted using GROMACS v2022.3 (University of Groningen, Netherlands, 2022) with the CHARMM36 force field applied to proteins and ligand topologies generated via the CGenFF server v2.5 (University of Maryland, USA, 2020). [32,33] Each complex was solvated in a cubic box using TIP3P water molecules and neutralized by adding appropriate counterions. Energy minimization was conducted using the steepest descent algorithm to remove bad contacts, followed by equilibration under NVT (100 ps) and NPT (100 ps) ensembles. The production run was performed for 200 ns at 310 K and 1 bar using the velocity-rescaling thermostat and Parrinello-Rahman barostat. Periodic boundary conditions were applied in all directions, and the Particle Mesh Ewald method was used for long-range electrostatics. LINCS constraints were applied to all bonds involving hydrogen atoms, allowing a 2 fs time step. The trajectory files were analyzed for root mean square deviation (RMSD) to assess structural fluctuations of the complexes. Additionally, MM-PBSA calculations were carried out using the g_mmpbsa tool v1.6.1 (Kumari et al., 2014) on 100 evenly spaced frames from the trajectory. [34] The decomposition of binding energy included van der Waals, electrostatic, polar solvation, and solvent-accessible surface area (SASA), contributions for each complex.

## Results and Discussion

*Molecular Docking Study of Natural Metabolites*

The molecular docking analysis involved selected metabolites from *Mitragyna speciosa* retrieved from the KNAPSACK database, evaluated against EBNA1 (6VH6 and 6NPP) and HPV E6 (6SJV) (Table 1). The binding affinity values varied across the compounds and targets, ranging from –4.65 to –11.2 kcal/mol. Acetylusulosic acid demonstrated the strongest binding to HPV E6 (6SJV), achieving a score of –11.2 kcal/mol, indicating strong interaction potential. Oleanolic acid also showed strong binding across all three proteins, particularly to HPV E6 (–10.8 kcal/mol), and with good affinities to EBNA1 (–8.1 kcal/mol for 6VH6 and –8.0 kcal/mol for 6NPP). Quercetin-3-rutinoside consistently exhibited high affinity, with docking scores of –8.0 kcal/mol (6VH6), –7.6 kcal/mol (6NPP), and –9.1 kcal/mol (6SJV). *β*-Stigmasterol exhibited similar performance, especially toward HPV E6 (–9.8 kcal/mol), while also maintaining strong interaction with EBNA1 targets. In contrast, 3-O-beta-D-Glucopyranosyl sitosterol showed weaker affinity to EBNA1 (–6.58 kcal/mol for 6VH6 and –4.65 kcal/mol for 6NPP) but strong interaction with HPV E6 (–9.9 kcal/mol). Several alkaloids, including Speciociliatine, Speciogynine, and Paynantheine, demonstrated moderate binding, ranging from –6.5 to –7.5 kcal/mol. Compounds like Corvnoxine B and Isomitraphylline recorded weak binding across all targets, indicating lower interaction potential. These results show that HPV E6 (6SJV) tended to yield stronger binding across a wider range of compounds compared to the EBNA1 structures.

The comparative docking profiles suggest that some *Mitragyna speciosa* metabolites possess broad-spectrum binding potential, while others show more target-specific interactions. Notably, Quercetin-3-rutinoside, Oleanolic acid, and *β*-Stigmasterol were among the most consistent performers, showing strong binding to both EBNA1 and HPV E6. Mitralactonal displayed moderate yet balanced affinity across the three proteins, with scores ranging from –6.99 to –7.85 kcal/mol.

**Table 1:** Docking scores of natural metabolites from *Mitragyna speciosa* against HPV E6 and EBNA1 target proteins using AutoDock Vina

| Metabolite | Molecular Formula | Molecular Weight | Docking Score (kcal/mol) | | |
|---|---|---|---|---|---|
| | | | EBNA1 (6VH6) | EBNA1 (6NPP) | HPV E6 (6SJV) |
| Caffeic acid | $C_9H_8O_4$ | 180.0422587 | -6.3 | -6.6 | -7.1 |
| (-)-Epicatechin | $C_{15}H_{14}O_6$ | 290.0790382 | -7.5 | -6.6 | -8.8 |
| Mitragynine | $C_{23}H_{30}N_2O_4$ | 398.2205575 | -5.9 | -6 | -7.1 |
| 3-O-Caffeoylquinic acid | $C_{16}H_{18}O_9$ | 354.0950822 | -7.2 | -6.2 | -7.8 |
| (-)-beta-Sitosterol | $C_{29}H_{50}O$ | 414.3861662 | -7.4 | -7.2 | -7.3 |
| *β*-Stigmasterol | $C_{29}H_{48}O$ | 412.3705162 | -8 | -8.4 | -9.8 |
| Apigenin | $C_{15}H_{10}O_5$ | 270.0528234 | -7.4 | -6.7 | -8.5 |
| Kaempferol | $C_{15}H_{10}O_6$ | 286.0477381 | -6.9 | -6.3 | -8.5 |
| Quercetin | $C_{15}H_{10}O_7$ | 302.0426527 | -6.8 | -6.7 | -8.3 |
| Hyperin | $C_{21}H_{20}O_{12}$ | 464.0954761 | -8 | -7.1 | -7.9 |
| Hirsutrin | $C_{21}H_{20}O_{12}$ | 464.0954761 | -7.5 | -6.3 | -8.1 |
| Quercetin 3-O-alpha-L-rhamnoside | $C_{21}H_{20}O_{11}$ | 448.1005615 | -7.9 | -7 | -8.2 |
| Quercetin 3-rutinoside | $C_{27}H_{30}O_{16}$ | 610.1533849 | -8 | -7.6 | -9.1 |
| Sweroside | $C_{16}H_{22}O_9$ | 358.1263823 | -6.9 | -6.5 | -7.6 |
| Vogeloside | $C_{17}H_{24}O_{10}$ | 388.136947 | -6.2 | -5.8 | -7.2 |
| Oleanolic acid | $C_{30}H_{48}O_3$ | 456.3603454 | -8.1 | -8 | -10.8 |
| 3-O-beta-D-Glucopyranosyl sitosterol | $C_{35}H_{60}O_6$ | 576.4389897 | -8.1 | -7.9 | -9.9 |
| 3-Isoajmalicine | $C_{21}H_{24}N_2O_3$ | 352.1786927 | -8.8 | -8.3 | -7.2 |
| Ciliaphylline | $C_{23}H_{30}N_2O_5$ | 414.2154721 | -6.3 | -6.2 | -7 |
| Corynantheidine | $C_{22}H_{28}N_2O_3$ | 368.2099928 | -6.1 | -6.3 | -7.6 |
| Corynoxeine | $C_{22}H_{26}N_2O_4$ | 382.1892573 | -6.7 | -5.7 | -6.7 |
| Corynoxine | $C_{22}H_{28}N_2O_4$ | 384.2049074 | -6 | -6.2 | -6.9 |
| Corynoxine B | $C_{22}H_{28}N_2O_4$ | 384.2049074 | -6.3 | -5.6 | -6.6 |
| Isocorynantheidine | $C_{22}H_{28}N_2O_3$ | 368.2099928 | -7.9 | -5.8 | -7.6 |
| Isomitrafoline | $C_{22}H_{28}N_2O_5$ | 400.199822 | -6.6 | -6 | -7.3 |
| Isomitraphylline | $C_{21}H_{24}N_2O_4$ | 368.1736073 | -7.1 | -6.9 | -7.4 |
| Isopaynantheine | $C_{23}H_{28}N_2O_4$ | 396.2049074 | -6.4 | -5.8 | -7.4 |

**ISSN 2616-0684 (Print)**
**ISSN 2616-0692 (Electronic)**

| | | | | | |
|---|---|---|---|---|---|
| Isorhynchophylline | $C_{22}H_{28}N_2O_4$ | 384.2049074 | -7.6 | -6.7 | -7 |
| Javaphylline | $C_{22}H_{26}N_2O_5$ | 398.184172 | -7.1 | -6.9 | -7.7 |
| Mitrafoline | $C_{22}H_{28}N_2O_5$ | 400.199822 | -6.6 | -6 | -7.5 |
| Mitragynine oxindole A | $C_{23}H_{30}N_2O_5$ | 414.2154721 | -5.9 | -5.7 | -7.5 |
| Mitragynine oxindole B | $C_{23}H_{30}N_2O_5$ | 414.2154721 | -6.2 | -6.1 | -6.1 |
| Mitrajavine | $C_{22}H_{26}N_2O_4$ | 382.1892573 | -6.7 | -8.3 | -6.7 |
| Paynantheine | $C_{23}H_{28}N_2O_4$ | 396.2049074 | -6.6 | -7 | -8.4 |
| Rhynchociline | $C_{23}H_{30}N_2O_5$ | 414.2154721 | -6.2 | -6 | -7 |
| Speciociliatine | $C_{23}H_{30}N_2O_4$ | 398.2205575 | -5.9 | -5.8 | -6.8 |
| Speciofoline | $C_{22}H_{28}N_2O_5$ | 400.199822 | -6.9 | -5.9 | -6.7 |
| Speciogynine | $C_{23}H_{30}N_2O_4$ | 398.2205575 | -6.5 | -6 | -9.2 |
| Specionoxeine | $C_{23}H_{28}N_2O_5$ | 412.199822 | -6.2 | -6.2 | -6.7 |
| Speciophylline | $C_{21}H_{24}N_2O_4$ | 368.1736073 | -6.6 | -6.4 | -7.9 |
| (6S,9R)-Roseoside | $C_{19}H_{30}O_8$ | 386.1940679 | -6.5 | -6.4 | -8.4 |
| Acetylursolic acid | $C_{32}H_{50}O_4$ | 498.3709101 | -7.4 | -7.3 | -11.2 |
| Corynantheidaline | $C_{21}H_{22}N_2O_3$ | 350.1630426 | -7 | -7 | -8 |
| Isocorynoxeine | $C_{22}H_{26}N_2O_4$ | 382.1892573 | -7.7 | -6.6 | -7.1 |
| Mitragynaline | $C_{22}H_{24}N_2O_4$ | 380.1736073 | -6.9 | -8.1 | -8.3 |
| Mitragynalinic acid | $C_{22}H_{24}N_2O_5$ | 396.1685219 | -6.4 | -6.4 | -7.6 |
| Mitralactonal | $C_{21}H_{20}N_2O_4$ | 364.1423071 | -8.6 | -8.5 | -8.7 |
| Mitralactonine | $C_{21}H_{20}N_2O_4$ | 364.1423071 | -7 | -8.2 | -8.9 |
| Mitrasulgynine | $C_{23}H_{28}N_2O_7S$ | 476.161722 | -6.8 | -6 | -7.6 |
| 7alpha-Hydroxy-7H-mitragynine | $C_{23}H_{30}N_2O_5$ | 414.2154721 | -7.2 | -7 | -7.9 |
| 9-Methoxymitralactonine | $C_{22}H_{22}N_2O_5$ | 394.1528718 | -7.2 | -8.2 | -8.9 |
| Epivogeloside | $C_{17}H_{24}O_{10}$ | 388.136947 | -6.2 | -6.1 | -8.4 |
| 7beta-Hydroxy-7H-mitraciliatine | $C_{23}H_{30}N_2O_5$ | 414.2154721 | -6.5 | -6.3 | -8.8 |
| Isospeciofoleine | $C_{22}H_{26}N_2O_5$ | 398.184172 | -6.4 | -6.1 | -7.1 |
| Isospeciofoline | $C_{22}H_{28}N_2O_5$ | 400.199822 | -6.4 | -6.1 | -6.3 |
| Isorotundifoline | $C_{22}H_{28}N_2O_5$ | 400.199822 | -6.4 | -6.1 | -7.2 |
| 7-Hydroxyspeciociliatine | $C_{23}H_{30}N_2O_5$ | 414.2154721 | -6.6 | -5.9 | -7.3 |

Several alkaloids such as Corvnoxeine and Isomitraphylline yielded less favorable scores, suggesting weaker interactions and lower suitability as inhibitors. Interestingly, 3-Isoajmalicine recorded a strong docking score with EBNA1 (6VH6) at –8.8 kcal/mol, while being less effective on the other targets. The EBNA1 model 6NPP generally exhibited slightly weaker interactions than 6VH6, possibly due to structural variations in the binding sites. Across all compounds, HPV E6 (6SJV) appeared to provide more favorable binding environments, resulting in lower (better) docking scores. These findings emphasize the importance of evaluating both structural diversity and target compatibility in early-stage virtual screening. The initial docking data support further computational validation of top-performing compounds. Ultimately, the KNAPSACK-derived metabolites of *Mitragyna speciosa* demonstrate promising interaction potential with viral oncogenic proteins relevant to cervical cancer.

*Binding Affinity and Inhibition Constant Analysis*

Based on the initial docking results using AutoDock Vina, five metabolites from *Mitragyna speciosa* were selected for further analysis due to their strong and consistent binding profiles. These compounds included 3-O-beta-D-Glucopyranosyl sitosterol, *β*-Stigmasterol, Mitralactonal, Oleanolic acid, and Quercetin-3-rutinoside. The binding energies and inhibition constants of these compounds against EBNA1 (6VH6 and 6NPP) and HPV E6 (6SJV) were evaluated using AutoDock Tools, as presented in Table 2. Against EBNA1 (6VH6), Oleanolic acid exhibited the strongest interaction with a binding energy of –8.78 kcal/mol and an inhibition constant of 363.94 nM. *β*-Stigmasterol also showed strong binding with a docking score of –8.25 kcal/mol and a Ki of 893.18 nM. Mitralactonal displayed a moderate affinity at –7.58 kcal/mol with a Ki of 2.78 µM. In contrast, 3-O-beta-D-Glucopyranosyl sitosterol had a weaker interaction, with –6.58 kcal/mol and a Ki of 15.10 µM.

**Table 2:** Binding energies and inhibition constants of selected *Mitragyna speciosa* metabolites against HPV E6 and EBNA1 targets using AutoDock Tools

| Selected Metabolite | EBNA1 (6VH6) | | EBNA1 (6NPP) | | HPV E6 (6SJV) | |
|---|---|---|---|---|---|---|
| | **Binding Energy (kcal/mol)** | **Inhibition Constant** | **Binding Energy (kcal/mol)** | **Inhibition Constant** | **Binding Energy (kcal/mol)** | **Inhibition Constant** |
| 3-O-beta-D-Glucopyranosyl sitosterol | -6.58 | 15.10 uM (micromolar) | -4.65 | 390.16 uM (micromolar) | -9.46 | 116.52 nM (nanomolar) |
| *β*-Stigmasterol | -8.25 | 893.18 nM (nanomolar) | -7.57 | 2.81 uM (micromolar) | -10.48 | 20.69 nM (nanomolar) |
| Mitralactonal | -7.58 | 2.78 uM (micromolar) | -6.99 | 7.47 uM (micromolar) | -7.85 | 1.76 uM (micromolar) |
| Oleanolic acid | -8.78 | 363.94 nM (nanomolar) | -8.31 | 811.49 nM (nanomolar) | -9.65 | 84.49 nM (nanomolar) |
| Quercetin-3-rutinoside | -4.62 | 410.21 uM (micromolar) | -4.04 | 1.09 mM (millimolar) | -7.12 | 6.07 uM (micromolar) |

**ISSN 2616-0684 (Print)**
**ISSN 2616-0692 (Electronic)**

Quercetin-3-rutinoside recorded the lowest affinity among the five, with a docking score of –4.62 kcal/mol and Ki of 410.21 µM. For EBNA1 (6NPP), overall binding energies were slightly less favourable. *β*-Stigmasterol remained the best binder with –7.57 kcal/mol and a Ki of 2.81 µM. Mitralactonal followed with –6.99 kcal/mol and a Ki of 7.47 µM. The remaining compounds showed higher inhibition constants, indicating weaker interactions with this conformation of EBNA1. All five compounds demonstrated stronger binding affinity toward HPV E6 (6SJV) compared to the two EBNA1 targets. *β*-Stigmasterol achieved the best docking score at –10.48 kcal/mol with an inhibition constant of 20.69 nM. Oleanolic acid followed with a binding energy of –9.65 kcal/mol and Ki of 84.49 nM. 3-O-beta-D-Glucopyranosyl sitosterol also exhibited a strong interaction, scoring –9.46 kcal/mol with a Ki of 116.52 nM. Mitralactonal yielded –7.85 kcal/mol and a Ki of 1.76 µM, indicating moderate binding strength. Quercetin-3-rutinoside had the weakest binding to HPV E6 among the five, with –7.12 kcal/mol and a Ki of 6.07 µM. Despite this, its binding to HPV E6 was notably stronger than to either EBNA1 structure. These results suggest that the active site of HPV E6 is more structurally compatible with the selected metabolites. The low nanomolar Ki values observed in *β*-Stigmasterol and Oleanolic acid support their role as promising binders. Quercetin-3-rutinoside, although less potent, showed target-dependent variability. Differences in binding energy across targets likely reflect conformational or physicochemical variations in each protein. Collectively, the AutoDock Tools analysis supports the docking trends observed previously and provides a clearer view of inhibitory potential based on both affinity and Ki.

*Molecular Interaction Profile Based on Hydrogen Bonds and Hydrophobic Contacts*

The molecular interaction analysis provided a detailed view of the binding behavior between the selected *Mitragyna speciosa* metabolites and the three viral protein targets. Table 3 summarizes the hydrogen bonds and hydrophobic contacts observed using BIOVIA Discovery Studio Visualizer. In the EBNA1 (6VH6) complex, 3-O-beta-D-Glucopyranosyl sitosterol formed five hydrogen bonds involving residues B:LYS477, B:LYS586, B:PRO587, B:PRO589, and B:ILE481. It also established one hydrophobic contact with B:THR515.

**Table 3:** Molecular interaction analysis of *Mitragyna speciosa* metabolites with HPV E6 and EBNA1 proteins based on BIOVIA Discovery Studio Visualizer

| Selected Metabolite | EBNA1 (6VH6) | | EBNA1 (6NPP) | | HPV E6 (6SJV) | |
|---|---|---|---|---|---|---|
| | Hydrogen Bonds | Hydrophobic Contacts | Hydrogen Bonds | Hydrophobic Contacts | Hydrogen Bonds | Hydrophobic Contacts |
| 3-O-beta-D-Glucopyranosyl sitosterol | B:LYS477, B:LYS586, B:PRO587, B:PRO589, B:ILE481 | B:THR515 | - | B:ILE481, B:ILE48, B:ILE582, B:ILE582, B:VAL583, B:LYS586, B:LYS586 | A:LYS16, A:LYS16, A:TRP63, A:ALA64, A:ASP66, A:GLU112, A:ASP15, A:TRP63 | - |
| *β*-Stigmasterol | B:ARG594 | B:LYS580, B:MET584, B:CYS591 | - | B:ILE481, B:LEU582, B:LYS586, B:LYS586, B:PRO589, B:PRO589, B:ILE481, B:LEU582 | - | A:TYR211, A:TRP341, A:PRO155, A:TYR156, A:PHE157, A:TYR211, A:TRP231, A:TRP341, A:TRP341 |
| Mitralactonal | B:LYS477, B:ASN519 | B:ILE481, B:LEU582, B:ILE481, B:LEU520 | B:LYS477, B:VAL583, B:ASN519 | B:LEU582, B:LYS586, B:ILE481, B:LEU520 | A:ASN13, A:ARG67, A:ARG67, A:GLU45, A:GLU154, | A:TRP63, A:TRP341, A:TRP341, A:TRP63, A:TRP63, A:TYR156 |
| Oleanolic acid | - | - | B:LYS477, B:ASN519 | - | A:ARG67, A:ASN151, A:ASP66 | A:TYR211, A:TRP341 |
| Quercetin-3-rutinoside | B:ASN480, B:SER516 | B:ILE481, B:ILE481, B:LEU520, B:LYS586, B:LYS586 | B:LYS477, B:LYS477, B:LYS586, B:SER516, B:LYS586 | B:ILE481, B:ILE481, B:LEU520, B:LEU582, B:VAL583, B:LYS586 | A:ASN13, A:ASN13, A:LYS16, A:LYS43, A:GLU112, A:GLU112, A:ASP15, A:GLU45, A:GLU46 | A:TRP63, A:LYS43 |

*β*-Stigmasterol formed a single hydrogen bond with B:ARG594 and established three hydrophobic interactions with B:LYS580, B:MET584, and B:CYS591. Mitralactonal engaged in two hydrogen bonds with B:LYS477 and B:ASN519, along with multiple hydrophobic contacts with B:ILE481, B:LEU582, B:ILE481, and B:LEU520. Oleanolic acid did not form hydrogen bonds with 6VH6 but showed weak hydrophobic interaction. Quercetin-3-rutinoside, on the other hand, formed hydrogen bonds with B:ASN480 and B:SER516 and formed hydrophobic contacts with B:ILE481, B:LEU520, B:LYS586, and B:SER516. For EBNA1 (6NPP), interaction patterns were generally similar but slightly varied in the number and type of residues involved. *β*-Stigmasterol and Quercetin-3-rutinoside showed interactions with recurring residues like B:ILE481, B:LEU582, and B:LYS586. Notably, Oleanolic acid and Mitralactonal both formed hydrogen bonds with B:LYS477 and B:ASN519. The data showed that residues B:LYS586, B:ILE481, and B:LEU582 are commonly involved

ISSN 2616-0684 (Print)
ISSN 2616-0692 (Electronic)

in hydrophobic contacts across multiple ligands. These findings indicate that EBNA1 binding is stabilized through repeated interaction at conserved residues.

For the HPV E6 target (6SJV), the compounds exhibited more extensive hydrogen bonding and hydrophobic interactions compared to EBNA1. 3-O-beta-D-Glucopyranosyl sitosterol formed hydrogen bonds with A:LYS16, A:TRP63, A:ALA64, A:ASP66, A:GLU112, and A:ASP15. It also engaged in hydrophobic contacts with A:TRP63. *β*-Stigmasterol interacted with multiple residues, forming contacts with A:TYR211, A:TRP341, A:PRO155, A:TYR156, A:PHE157, A:TRP231, and multiple contacts with A:TRP341. Mitralactonal formed hydrogen bonds with A:ASN13, A:ARG67, A:GLU45, and A:GLU154, while its hydrophobic interactions were dominated by A:TRP63 and A:TYR156. Oleanolic acid formed hydrogen bonds with A:ARG67, A:ASN151, and A:ASP66, and maintained hydrophobic contact with A:TRP341 and A:TYR211. Quercetin-3-rutinoside established extensive hydrogen bonding with residues A:ASN13, A:ASN16, A:LYS16, A:GLU112, A:ASP15, A:VAL583, and A:GLU46. Its hydrophobic interactions involved A:TRP63 and A:LYS43. Across the five compounds, A:TRP63 and A:GLU112 were the most frequently involved residues, indicating their significance in ligand binding to HPV E6. These recurring contacts suggest the existence of a structurally favorable pocket on HPV E6 that promotes multi-point binding. The diverse bonding profiles of the metabolites highlight their unique modes of interaction with the protein target. Compounds with both hydrogen and hydrophobic interactions tended to exhibit stronger docking scores in earlier stages. These structural findings align with and reinforce the binding affinity trends obtained in previous docking and scoring results.

*In Silico ADME and Bioavailability Profiling of Selected Metabolites*

The *in silico* ADME profiling of the five selected *Mitragyna speciosa* metabolites was evaluated using SwissADME (Table 4).

**Table 4:** *In silico* ADME profiling of selected *Mitragyna speciosa* metabolites based on physicochemical and pharmacokinetic properties

| Selected Metabolite | TPSA (Å²) | Consensus LogP | ESOL Solubility Class | GI Absorption | BBB Permeant | P-gp Substrate | Bioavailability Score |
|---|---|---|---|---|---|---|---|
| 3-O-beta-D-Glucopyranosyl sitosterol | 99.38 | 5.55 | Poorly soluble | Low | No | No | 0.55 |
| *β*-Stigmasterol | 20.23 | 6.98 | Poorly soluble | Low | No | No | 0.55 |
| Mitralactonal | 71.63 | 2.46 | Soluble | High | Yes | No | 0.55 |
| Oleanolic acid | 57.53 | 6.07 | Poorly soluble | Low | No | No | 0.85 |
| Quercetin-3-rutinoside | 269.43 | -1.20 | Soluble | Low | No | Yes | 0.11 |

The physicochemical and pharmacokinetic properties assessed include topological polar surface area (TPSA), consensus LogP, solubility, gastrointestinal (GI) absorption, blood–brain barrier (BBB) permeability, P-glycoprotein substrate status, and bioavailability score. Among the five compounds, Quercetin-3-rutinoside exhibited the highest TPSA value at 269.43 Å², which is well above the threshold for optimal oral absorption. In contrast, *β*-Stigmasterol had the lowest TPSA at 20.23 Å², indicating higher membrane permeability potential. The LogP values also varied, with *β*-Stigmasterol and Oleanolic acid having the highest lipophilicity at 6.98 and 6.07, respectively. Quercetin-3-rutinoside was the only compound with a negative LogP value (–1.20), indicating greater hydrophilicity. In terms of solubility, all compounds except Mitralactonal and Quercetin-3-rutinoside were predicted to be poorly soluble. Mitralactonal showed favorable pharmacokinetics with high GI absorption and positive BBB permeability, suggesting systemic availability after oral administration. The remaining compounds had low predicted GI absorption and were not permeant to the BBB. Only Quercetin-3-rutinoside was predicted to be a substrate of P-glycoprotein, which may affect its efflux and bioavailability. Oleanolic acid had the highest predicted bioavailability score of 0.85, while Quercetin-3-rutinoside had the lowest at 0.11.

The bioavailability radar plots for the five compounds are presented in Figure 1, providing a visual representation of six critical properties: lipophilicity (LIPO), size, polarity (POLAR), solubility (INSOLU), saturation (INSATU), and molecular flexibility (FLEX). Each radar plot is enclosed by a pink shaded region that represents the optimal range for oral bioavailability. 3-O-beta-D-Glucopyranosyl sitosterol exhibited good balance in LIPO and FLEX, but extended beyond optimal limits in polarity and size. *β*-Stigmasterol showed a compact and centered profile, especially within the LIPO and SIZE axes, but was slightly outside the ideal POLAR and INSOLU regions. Mitralactonal had the most compact profile among all, closely fitting within the shaded zone, which correlates with its favorable GI absorption and BBB permeability. Oleanolic acid also remained largely within the optimal boundaries, with only minor deviation in solubility. In contrast,

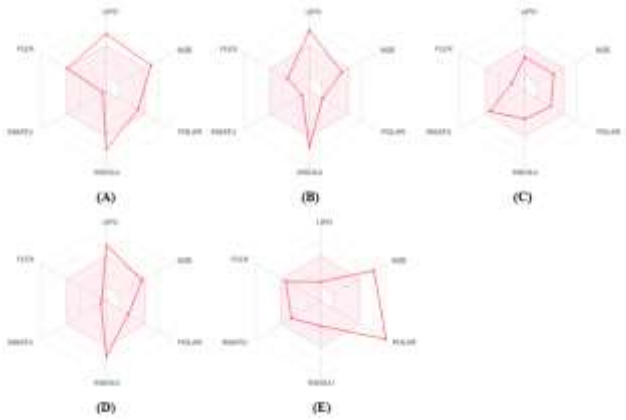


**Figure 1:** Bioavailability radar profiles of selected *Mitragyna speciosa* metabolites based on SwissADME parameters: (A) 3-O-beta-D-Glucopyranosyl sitosterol, (B) *β*-Stigmasterol, (C) Mitralactonal, (D) Oleanolic acid, and (E) Quercetin-3-rutinoside.

Quercetin-3-rutinoside extended far beyond the optimal range in polarity and size, reflecting its high TPSA and low bioavailability. The radar visualization complements the tabulated data by highlighting the trade-offs between lipophilicity, solubility, and molecular size. Compounds that fell largely within the pink zone, such as Mitralactonal and Oleanolic acid, are more likely to exhibit favorable oral bioavailability. Meanwhile, the broad and uneven spread of Quercetin-3-rutinoside suggests limited permeability and absorption. These results provide additional context to the docking data by identifying compounds with both good binding affinity and suitable pharmacokinetic properties. Together, they assist in prioritizing compounds for further in vitro testing based on both interaction potential and ADME behavior.

ISSN 2616-0684 (Print)
ISSN 2616-0692 (Electronic)

*In Silico Oral Toxicity Prediction of Selected Metabolites*

Oral toxicity prediction was conducted to assess the toxicological profile of the five *Mitragyna speciosa* metabolites (Figure 2). The predicted $LD_{50}$ values ranged from 890 mg/kg to 8000 mg/kg, corresponding to toxicity classes 4 to 6. 3-O-beta-D-Glucopyranosyl sitosterol exhibited the highest $LD_{50}$ value of 8000 mg/kg, classified as toxicity class 6, indicating it is relatively non-toxic. This compound demonstrated amoderate average similarity of 79.06% and a prediction accuracy of 69.26%. In contrast, *β*-Stigmasterol displayed a much lower $LD_{50}$ of 890 mg/kg and was categorized into class 4, implying moderate toxicity.

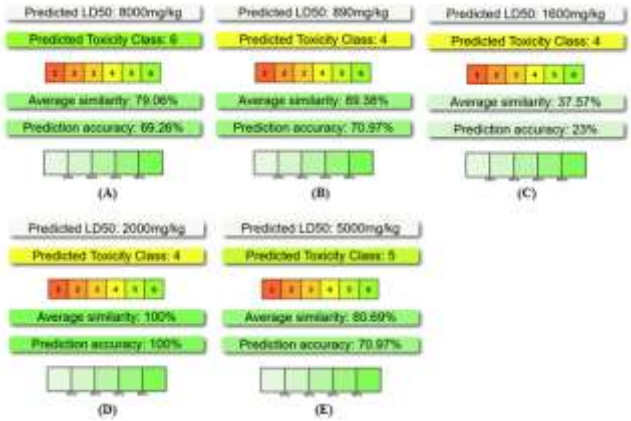


**Figure 2:** Predicted oral toxicity profiles of selected *Mitragyna speciosa* metabolites based on $LD_{50}$ and toxicity class: (A) 3-O-beta-D-Glucopyranosyl sitosterol, (B) *β*-Stigmasterol, (C) Mitralactonal, (D) Oleanolic acid, and (E) Quercetin-3-rutinoside.

Its prediction was supported by high similarity (89.38%) and prediction accuracy of 70.97%. Mitralactonal had an $LD_{50}$ of 1600 mg/kg and shared the same toxicity class 4, but with lower model confidence reflected by a similarity of only 37.57% and 23% prediction accuracy. Oleanolic acid had an $LD_{50}$ of 2000 mg/kg and also belonged to class 4, but it showed perfect similarity and prediction accuracy, both at 100%. This indicates strong confidence in its moderate toxicity level. Quercetin-3-rutinoside showed an $LD_{50}$ of 5000 mg/kg, classified into class 5, suggesting it may have low to moderate toxicity. Its prediction was relatively reliable with an 80.69% similarity and 70.97% accuracy. The variation in prediction confidence highlights the importance of evaluating both toxicity class and model performance metrics. The toxicity class scale used in this study ranged from 1 (most toxic) to 6 (least toxic), providing a clear qualitative measure of potential harm. 3-O-beta-D-Glucopyranosyl sitosterol was the only compound categorized in class 6, identifying it as the least toxicamong the selected metabolites. Compounds in class 4 such as *β*-Stigmasterol, Mitralactonal, and Oleanolic acid are considered to have moderate toxicity and require cautious evaluation before further use. Despite sharing the same class, these compounds vary in their confidence levels, suggesting differences in structural similarity with training data. Mitralactonal, for instance, had the lowest confidence values, possibly due to its distinct chemical scaffold. In contrast, Oleanolic acid stood out for its perfect model match, reinforcing its toxicity classification. The intermediate toxicity of Quercetin-3-rutinoside placed it in class 5, suggesting lower toxicity than class 4 compounds but still warranting observation. These findings are particularly important in the context of drug development where oral safety is a major determinant of clinical translation. The predicted $LD_{50}$ values also aid in approximating therapeutic index when compared with binding or effective concentrations. Although *in silico* toxicity does not substitute in vivo evaluation, it offers an efficient first-tier screening. Generally, these results help identify compounds with favorable therapeutic margins. Further experimental validation is essential to confirm these computational predictions in biological models.

*Molecular Dynamics Simulation of Ligand-Protein Complexes*

To complement the oral toxicity predictions, molecular dynamics (MD) simulations were performed to assess the structural stability of selected metabolite–protein complexes. Figure 3 shows the RMSD profiles of native and ligand-bound forms of EBNA1 (PDB IDs: 6VH6 and 6NPP) and HPV E6 (6SJV) over 200 ns trajectories. Oleanolic acid reduced RMSD values of EBNA1 (6VH6) from native levels of 0.3–0.4 nm to approximately 0.22–0.25 nm, indicating improved conformational stability.

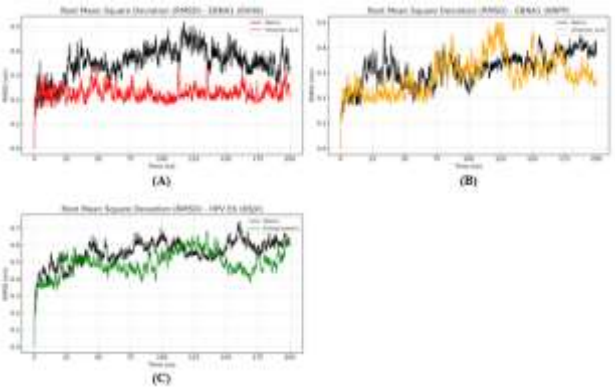


**Figure 3:** Root Mean Square Deviation (RMSD) profiles of native-ligand complexes during 200 ns molecular dynamics simulations: (A) EBNA1 (6VH6) with oleanolic acid, (B) EBNA1 (6NPP) with oleanolic acid, and (C) HPV E6 (6SJV) with *β*-Stigmasterol.

A similar stabilizing effect was observed when EBNA1 (6NPP) in complex with oleanolic acid displayed RMSD curves that closely followed the native, with slightly smoother fluctuations. This consistency across two EBNA1 conformations supports oleanolic acid's structural compatibility. Notably, oleanolic acid demonstrated100% similarity and accuracy in oral toxicity modeling, reinforcing its potential safety and efficacy. Meanwhile, *β*-Stigmasterol stabilized HPV E6 (6SJV), lowering RMSD values relative to the native form, with fewer deviations above 0.6 nm. Although *β*-Stigmasterol had a lower $LD_{50}$ (890 mg/kg), it maintained acceptable structural dynamics in the binding pocket. These findings demonstrated that both ligands effectivelystabilize their targets while preserving native-like dynamics. Stable RMSD profiles suggest persistent binding and low likelihood of protein misfolding or ligand dissociation. Furthermore, the MD results align with toxicity predictions and support the compounds' drug-likeness.

The RMSD stability of these complexes also reflects key pharmacodynamic advantages. Oleanolic acid exhibited robust performance by stabilizing two EBNA1 structures without inducing significant perturbation, making it suitable for a broad-spectrum antiviral scaffold. *β*-Stigmasterol, while slightly more toxic, showed strong binding-induced stabilization of HPV E6, a critical oncoprotein in cervical cancer. The differential performance of these ligands across targets illustrates their unique conformational effects and potential selectivity. RMSD profiles over time reveal that none of the compounds introduced erratic fluctuations, which could signal unfavorable interactions. The observed stability implies favorable enthalpic and entropic contributions to binding. Moreover, these results help bridge the gap between computational toxicity estimation and dynamic behavior in biologically relevant contexts. The RMSD consistency over 200 ns offers confidence in ligand retention and minimal distortion of protein structure. This is especially important for drug candidates aimed at modulating protein–protein or DNA–binding functions. In this context, the selected metabolites fulfill essential criteria for lead compound development, combining manageable toxicity with structural compatibility. Altogether, these RMSD findings provide foundational support for prioritizing oleanolic acid and *β*-Stigmasterol

in further antiviral and anticancer development pipelines.

*Binding Free Energy Analysis via MM-PBSA*

To evaluate the thermodynamic favorability of ligand binding, MM-PBSA calculations were conducted for selected metabolite–protein complexes (Table 5). For EBNA1 (6VH6), oleanolic acid exhibited a more negative total binding energy (–114.790 kJ/mol) compared to the native ligand QX4 (–78.333 kJ/mol), suggesting stronger binding affinity. This increase was mainly attributed toa more favorable van der Waals contribution (–142.666 vs –89.924 kJ/mol), indicating enhanced hydrophobic interactions.

**Table 5:** Binding free energy components of selected metabolites against EBNA1 and HPV E6 targets using MM-PBSA analysis

| Selected Metabolite | van der Waal energy (kJ/mol) | Electrostattic energy (kJ/mol) | Polar solvation energy (kJ/mol) | SASA energy (kJ/mol) | Binding energy (kJ/mol) |
|---|---|---|---|---|---|
| **EBNA1 (6VH6)** | | | | | |
| native (QX4) | -89.924 | -22.909 | 44.590 | -10.090 | -78.333 |
| Oleanolic acid | -142.666 | -12.948 | 55.245 | -14.420 | -114.790 |
| **EBNA1 (6NPP)** | | | | | |
| native (KWG) | -144.362 | -490.748 | 383.257 | -15.155 | -267.009 |
| Oleanolic acid | -131.015 | -41.016 | 85.685 | -13.910 | -100.257 |
| **HPV E6 (6SJV)** | | | | | |
| native (PRD) | -145.074 | -238.090 | 292.218 | -16.161 | -107.107 |
| *β*-Stigmasterol | -210.664 | -3.860 | 106.076 | -21.538 | -129.986 |

Electrostatic energy was also slightly improved (–12.948 vs –22.909 kJ/mol), and the SASA energy was more negative, indicating stronger surface contact. Although the polar solvation energy increased (55.245 vs 44.590 kJ/mol), which is generally unfavorable, the total binding energy still showed a net improvement. In EBNA1 (6NPP), however, the native ligand KWG retained a significantly more favorable electrostatic profile (–490.748 kJ/mol) than oleanolic acid (–41.016 kJ/mol), contributing to a stronger overall binding energy (–267.009 kJ/mol vs –100.257 kJ/mol). This significant difference suggests that the native ligand forms extensive polar interactions, possibly via charged residues or hydrogen bonds. Nonetheless, oleanolic acid still maintained a moderate binding profile with favorable van der Waals (–131.015 kJ/mol) and SASA contributions (–13.910 kJ/mol). These results imply that oleanolic acid may not fully replace the electrostatic efficiency of the native ligand in 6NPP, but it offers a more balanced binding mode. The MM-PBSA results for oleanolic acid reinforce its dual role as a moderately strong binder with acceptable dynamic and toxicity profiles. Thus, it remains a promising candidate for EBNA1 targeting, especially under hydrophobic interaction dominance. For HPV E6 (6SJV), *β*-Stigmasterol showed stronger binding affinity (–129.986 kJ/mol) compared to the native ligand PRD (–107.107 kJ/mol), underscoring its interaction potency. The enhanced affinity was primarily due to an improved van der Waals interaction (–210.664 vs –145.074 kJ/mol), signifying robust hydrophobic engagement within the binding pocket. Although the polar solvation energy of *β*-Stigmasterol was higher (106.076 kJ/mol vs 292.218 kJ/mol), indicating lower desolvation penalty, its electrostatic contribution was minimal (–3.860 kJ/mol) compared to the highly negative value of the native ligand (–238.090 kJ/mol). This reveals that *β*-Stigmasterol favors non-polar interactions while compromising electrostatic bonding. However, its SASA energy (–21.538 kJ/mol) was also more negative, suggesting improved solvent-accessible binding surface. The dominance of van der Waals and SASA terms hints that *β*-Stigmasterol fits tightly and stably in the hydrophobic core of HPV E6. Despite lower electrostatic engagement, the compound compensated through better shape complementarity and surface contact. This aligns well with its RMSD stability profile and supports its role as a hydrophobic binder. Compared to oral toxicity predictions, *β*-Stigmasterol still falls in class 4 but balances efficacy and stability effectively. Thus, MM-PBSA findings validate its dynamic behavior and justify further experimental testing. Altogether, the binding energy decomposition highlights distinct interaction mechanisms for each metabolite, offering insights for optimization strategies in future analog development.

## Conclusion

This study successfully identified promising antiviral candidates from *Mitragyna speciosa* against HPV E6 and EBNA1 using an integrated *in silico* approach. From 50 screened compounds, five top candidates showed strong binding affinities, stable interactions, and favorable inhibition profiles. Molecular dynamics simulations confirmed the stability of their complexes, while SwissADME and ProTox-II analyses indicated acceptable drug-likeness and predicted safety. Overall, *β*-stigmasterol and oleanolic acid emerged as the most promising scaffolds for further antiviral development.

## Conflict of Interest

The authors declare no conflict of interest.

## Authors' Declaration

The authors hereby declare that the work presented in this article is original and that any liability for claims relating to the content of this article will be borne by them.

## References

1. Blanco R, Carrillo-Beltrán D, Osorio JC, Calaf GM, Aguayo F. Role of Epstein-Barr virus and human papillomavirus coinfection in cervical cancer: epidemiology, mechanisms and perspectives. Pathogens. 2020; 9(3):1-17.
2. Shi Y, Peng SL, Yang LF, Chen X, Tao YG, Cao. Co-infection of Epstein-Barr virus and human papillomavirus in human tumorigenesis. Chinese Journal of Cancer. 2016; 35(16):1-9.
3. Gomez K, Schiavoni G, Nam Y, Reynier J-B, Khamnei C, Aitken M, Palmieri G, Cossu A, Levine A, van Noesel C, Falini B, Pasqualucci L, Tiacci E, Rabadan R. Genomic landscape of virus-associated cancers. medRxiv Prepr. Serv. Heal. Sci. 2023;1-44.
4. Kombe AJK, Li B, Zahid A, Mengist HM, Bounda GA, Zhou Y, Jin T. Epidemiology and Burden of Human Papillomavirus and Related Diseases, Molecular Pathogenesis, and Vaccine Evaluation. Frontiers in Public Health. 2021; 8:1-19.
5. Jakovljevic A, Andric M. Human cytomegalovirus and epstein-barr virus in etiopathogenesis of apical periodontitis: A systematic review. Journal of Endodontics. 2014; 40(1):6-10.
6. Grabarek, BO, Ossowki P, Czarniecka J, Ozog M, Prucnal J, Dziuba I, Ostenda A, Dziobek K, Boron D, Peszek W, Kras P, Januszyk S, Dabala M, Kasela T, Oplawski M. Detection and Genotyping of Human Papillomavirus (HPV16/18), Epstein–Barr Virus (EBV), and Human Cytomegalovirus (HCMV) in Endometrial Endometroid and Ovarian Cancers. Pathogens. 2023; 12(397):1-14.
7. Vranic S, Cyprian FS, Akhtar S, Al Moustafa AE. The role of Epstein-Barr virus in cervical cancer: A brief update. Frontiers in Oncology. 2018; 8(113):1-8.

8. Yim, EK, Park JS. The Role of HPV E6 and E7 Oncoproteins in HPV-associated Cervical Carcinogenesis. Cancer Res. Treat. 2005; 37(6):319-324.
9. Gutiérrez-Hoya A, Soto-Cruz I. Role of the JAK/STAT Pathway in Cervical Cancer: Its Relationship with HPV E6/E7 Oncoproteins. Cells. 2020; 9(2297):1-22.
10. DasGupta T, Nweze EI, Yue H, Wang L, Jin J, Ghosh SK, Kawsar HI, Zender C, Androphy EJ, Weinberg A, McCromick TS, Jin G. Human papillomavirus oncogenic E6 protein regulates human β-defensin 3 (hBD3) expression via the tumor suppressor protein p53. Oncotarget. 2016; 7(19):27430-27444.
11. Wilson JB, Manet E, Gruffat H, Busson P, Blondel M, Fahraeus R. EBNA1: Oncogenic activity, immune evasion and biochemical functions provide targets for novel therapeutic strategies against epstein-barr virus-associated cancers. Cancers. 2018; 10(109):1-30.
12. Boudreault S, Armero VES, Scott MS, Perreault JP, Bisaillon M. The Epstein-Barr virus EBNA1 protein modulates the alternative splicing of cellular genes. Virol. J. 2019; 16(29):1-14.
13. Zafar A, Khan MJ, Abu J, Naeem A. Revolutionizing cancer care strategies: immunotherapy, gene therapy, and molecular targeted therapy. Molecular Biology Reports. 2024; 51(219):1-14.
14. Jin H, Liao S, Yao F, Li J, Xu Z, Zhao K, Xu X, Sun S. Insight into the Crosstalk between Photodynamic Therapy and Immunotherapy in Breast Cancer. Cancers. 2023; 15(1532):1-24.
15. Tafrihani AS, Hanif N, Yoga IMBK, Iramasari I, Fakih TM, Novitasari D, Hasibuan PAZ, Satria D, Huda F, Muchtaridi M, Hermawan A. A computational study of cardiac glycosides from Vernonia amygdalina as PI3K inhibitors for targeting HER2 positive breast cancer. J. Comput. Aided. Mol. Des. 2025; 39(43):1-6.
16. Chaachouay N, Zidane L. Plant-Derived Natural Products: A Source for Drug Discovery and Development. Drugs Drug Candidates. 2024; 3(1):184-207.
17. Atanasov AG, Waltenberger B, Pferschy-Wenzig EM, Linder T, Wawrosch C, Uhrin P, Temmi V, Wang L, Schwaiger S, Heiss EH, Rollinger JM, Schuster D, Breuss JM, Bochkov V, Mihovilovic MD, Kopp B, Bauer R, Dirsch VM, & Struppner H . Discovery and resupply of pharmacologically active plant-derived natural products: A review. Biotechnology Advances. 2015; 33:1582-1614.
18. Akbar NH, Suarantika F, Fakih TM, Haniffadli A, Muslimawati K, Putra AMP. Screening, docking, and molecular dynamics analysis of *Mitragyna speciosa* (Korth.) compounds for targeting HER2 in breast cancer. Curr. Res. Struct. Biol. 2025; 10:1-13.
19. Ghazalli MN, Sah MSM, Mat M, Awang K, Jaafar MA, Mirad R, Zaini AZ, Nordin ARM, Rusli NM, Mohamad SS, Syahman A. Leaf anatomy and micromorphology characteristics of ketum [*Mitragyna speciosa* (Korth.) Havil.] (Rubiaceae). Trop. Life Sci. Res. 2021; 32(1):1-12.
20. Brose J, Lau KH, Dang TTT, Hamilton JP, Martins LDV, Hamberger B, Hamberger B, Jiang J, O'Connor SE, Buell CR. The *Mitragyna speciosa* (Kratom) Genome: A resource for data-mining potent pharmaceuticals that impact human health. G3 Genes, Genomes, Genet. 2021; 11(4):1-9.
21. Priatna PA, Pratama RR, Widyowati R, Sukardiman. Molecular Docking Estrogen Receptor Alpha Antagonist and P53-MDM2 Inhibitor, ADMET Prediction of Alkaloid Compound from *Mitragyna speciosa* for Breast Cancer Therapy. Pharmacogn. J. 2022; 14(6s):912-916.
22. Arief I, Inderiyani I. Virtual Screening to Identification The Active Compounds from Kratom (*Mitragyna speciosa*) as Analgetics. Pharmacon J. Farm. Indones. 2023; 20(2):1-10.
23. Afendi F, Okada T, Yamazaki M, Morita AH, Nakamura Y, Nakamura K, Ikeda S, Takahashi H, Amin A, Darusman LK, Saito K, Kanaya S. KNApSAcK family databases: integrated metabolite-plant species databases for multifaceted plant research. Plant Cell Physiol. 2012; 53(2):1-10.
24. Brown T. ChemDraw. *Sci. Teach.* 2014; 81(2).
25. Eberhardt J, Santos-Martins D, Tillack AF, Forli, S. AutoDock Vina 1.2.0: New Docking Methods, Expanded Force Field, and Python Bindings. J. Chem. Inf. Model. 2021; 61(6).
26. Morris GM, Goodsell DS, Pique ME, Lindstrom W, Huey R, Forli S, Hart WE, Halliday S, Belew R, Olson AJ. AutoDock Version 4.2. Citeseer. 2014; 15:30.
27. Messick TE, Tolvinski L, Zartler, ER, Moberg A, Frostell A, Smith GR, Reitz AB, Lieberman PM. Biophysical screens identify fragments that bind to the viral DNA-binding proteins EBNA1 and LANA. Molecules. 2020; 10(25):1-14.
28. Messick TE, Smith GR, Soldan SS, McDonnell ME, Deakyne JS, Malecka KA, Tolvinski L, Heuvel APJVD, Gu BW, Cassel JA, Tran DH, Wassermann BR, Zhang Y, Velvadapu V, Zartler ER, Busson P, Reitz AB, Lieberman PM. Structure-based design of small-molecule inhibitors of EBNA1 DNA binding blocks Epstein-Barr virus latent infection and tumor growth. Sci. Transl. Med. 2019; 11(482):1-27.
29. BIOVIA. Dassault Systèmes BIOVIA. Discovery Studio Modeling Environment. Dassault Systèmes San Diego. 2017.
30. Daina A, Michielin O, Zoete V. SwissADME: A free web tool to evaluate pharmacokinetics, drug-likeness and medicinal chemistry friendliness of small molecules. Sci. Rep. 2017; 7:1-13.
31. Banerjee P, Eckert, AO, Schrey AK, Preissner R. ProTox-II: A webserver for the prediction of toxicity of chemicals. Nucleic Acids Res. 2018; 46:257-263.
32. Abraham M, Alekseenko A, Bergh C, Blau C, Briand E, Doijade M, Fleischmann S, Gapsys V, Garg G, Gorelov S, Gouaillardet G, Gray A, Irrgang ME, Jalalypour F, Jordan J, Junghans C, Kanduri P, Keller S, Kutzner C, Lemkul JA, Lundborg M, Merz P, Miletic V, Morozov D, Pall S, Schulz R, Shirts M, Shvetsov A, Soproni B, Spoel DVD, Turner P, Uphoff C, Villa A, Wingbermuhle S, Zhmurov A, Bauer P, Hess B, Lindahl E. GROMACS 2023.3 Manual (2023.3). Zenodo. Gromacs manual-2023.3. 2023.
33. Abraham M, Murtola T, Schulz R, Pall S, Smith J, Hess B, Lindahl E. GROMACS: High performance molecular simulations through multi-level parallelism from laptops to supercomputers. SoftwareX. 2015; 1:19-25.
34. Kumari R, Kumar R, Consortium OSDD, Lynn A. g _ mmpbsa - A GROMACS tool for MM-PBSA and its optimization for high-throughput binding energy calculations. J. Chem. Inf. Model. 2014; 54(7):1-10.